Nano Research
2022, 15(3): 2023–2029
ISSN 1998-0124 CN 11-5974/O4
https://doi.org/10.1007/s12274-021-3738-8

Research Article

Conversion of hydroxide into carbon-coated phosphide using plasma for sodium ion batteries

Jin Liang[1], Guoyin Zhu[3], Yizhou Zhang[3,4] (✉), Hanfeng Liang[2] (✉), and Wei Huang[1,4] (✉)

[1] Key Laboratory of Flexible Electronics (KLOFE) & Institute of Advanced Materials (IAM), Nanjing Tech University (NanjingTech), Nanjing 211800, China
[2] College of Chemistry and Chemical Engineering, Xiamen University, Xiamen 361005, China
[3] School of Chemistry and Materials Science, Institute of Advanced Materials and Flexible Electronics (IAMFE), Nanjing University of Information Science and Technology, Nanjing 210044, China
[4] State Key Laboratory of Organic Electronics and Information Displays & Institute of Advanced Materials (IAM), Nanjing University of Posts & Telecommunications, Nanjing 210023, China

Received: 17 June 2021 / **Revised:** 7 July 2021 / **Accepted:** 10 July 2021

ABSTRACT

Transition metal phosphides (TMPs) are promising candidates for sodium ion battery anode materials because of their high theoretical capacity and earth abundance. Similar to many other P-based conversion type electrodes, TMPs suffer from large volumetric expansion upon cycling and thus quick performance fading. Moreover, TMPs are easily oxidized in air, resulting in a surface phosphate layer that not only decreases the electric conductivity but also hinders the Na ion transport. In this work, we present a general electrode design that overcomes these two major challenges facing TMPs. Using metal hydroxide and glucose as precursors, we show that the metal hydroxide can be converted into phosphide whereas the glucose simultaneously decomposes and forms carbon shell on the phosphide particles under a plasma ambient. Ni_2P@C core shell structures as a proof-of-concept are designed and synthesized. The *in situ* formed carbon shell protects the Ni_2P from oxidation. Moreover, the high-energy plasma introduces porosity and vacancies to the Ni_2P and more importantly produces phosphorus-rich nickel phosphides (NiP_x). As a result, the Ni_2P@C electrodes achieve high sodium capacity (693 $mAh\cdot g^{-1}$ after 50 cycles at 100 $mA\cdot g^{-1}$) and excellent cyclability (steady capacity maintained for at least 1, 500 cycles). Our work provides a general strategy for enhancing the sodium storage performance of TMPs, and in general many other conversion type electrode materials that are unstable in air and suffer from large volumetric changes upon cycling.

KEYWORDS

porous anodes, Ni_2P, plasma conversion, phosphorus-rich, sodium ion batteries

1 Introduction

Lithium-ion batteries (LIBs) have quickly dominated the power market of portable electronic devices since their first commercialization by SONY because of the high-energy density and long lifespan [1–5]. As the use of LIBs becomes widespread, concerns over Li supply have arisen. The low abundance of Li in the Earth's crust (only 20 ppm) would ultimately push up the price of Li and make large-scale grid storage prohibitively expensive. In this regard, sodium ion batteries (NIBs) promise a favorable alternative due to the greater abundance (by a factor of 10^3) and therefore lower cost of Na [6, 7]. However, the seemingly simple replacement of Li with Na causes drastic consequences for the resulting electrochemistry though these two metals have similar properties in many aspects. For example, the well-known anode materials for LIBs, such as graphite and silicon [8], show negligible capacities when used for NIBs [9]. Enormous efforts have thus been devoted toward exploring new electrode materials, ideally with high capacity and stability, to advance the NIBs technology.

Of all possible anodes for NIBs, elemental phosphorus probably is the most appealing material due to its low cost and extremely high capacity with a theoretical number of 2,596 $mAh\cdot g^{-1}$ (based on the conversion reaction of P to Na_3P) [10, 11]. Such a conversion reaction is inevitably accompanied by a massive volumetric expansion of ~ 400% that leads to significant capacity decay upon sodiation/desodiation [10, 11]. Moreover, P has a poor electric conductivity (~ 10^{-12} $S\cdot cm^{-1}$) and thus a slow reaction kinetics. Very large amounts of conductive carbons are typically needed to enhance the conductivity and the mechanical stability of P-based electrodes [10, 11]. This, however, decreases the gravimetric and volumetric energy densities. Introducing metals such as Ni (or more commonly Sn) into P to form intermetallic phosphides (e.g., Ni_2P) may potentially address the aforementioned issues of P-based anodes [12]. Although the theoretical gravimetric capacity of Ni_2P (542 $mAh\cdot g^{-1}$) is much lower than that of P, their theoretical volumetric capacities are comparable (4,032 $mAh\cdot g^{-1}$ for Ni_2P vs. 5,710 $mAh\cdot g^{-1}$ for P) [13]. The latter is perhaps an even more important metric for many applications such as electric vehicles, where the space is often more limiting

Address correspondence to Yizhou Zhang, yizhou.zhang@nuist.edu.cn; Hanfeng Liang, hfliang@xmu.edu.cn; hanfeng.liang@kaust.edu.sa; Wei Huang, wei-huang@njtech.edu.cn

than the weight of the batteries. Moreover, Ni_2P is a metal and its conductivity (2.4×10^8 S·cm^{-1}) [14] is significantly higher than that of P/C composites (3.5×10^{-5} S·cm^{-1}). Further, Ni_2P could possibly exhibit a pseudocapacitive behavior [15] that favors the high rate performance. These features make Ni_2P a promising anode material for NIBs. In fact, Ni_2P has been extensively investigated in LIBs [16–20], but unfortunately, has so far rarely been explored for NIBs. Like many other phosphide-based conversion type anodes (e.g., Cu_3P) [12, 21], one can expect that Ni_2P would also suffer from large volumetric expansion upon sodiation (as already observed in lithium insertion) [16], which induces pulverization of the electrode and thus the fast capacity fading. Delicate nanostructuring (e.g., nanowires, hollow spheres) appears to be an effective approach to address this problem to some degree [22, 23], however, achieving ultralong lifespan (> 1,000 cycles) of phosphide electrodes with steady capacity, especially at high rates, remains a big challenge. Another seemingly inconspicuous but practically important issue is that the Ni_2P (and metal phosphides in general) is easily oxidized in air to form a surface phosphate layer that not only decreases the conductivity but also hinders Na^+ transport, therefore raising additional challenge for achieving good electrochemical performance.

Herein, we demonstrate an electrode design that successfully overcomes the abovementioned two major challenges facing Ni_2P electrodes (and many other oxidation sensitive conversion type electrode materials such as nitrides) at the same time using plasma. Plasma has attracted increasing attention in the synthesis of various energy-related materials including transition metal nitrides, phosphides, chalcogenides, and oxides. Compared with other common synthetic methods, the plasma-assisted synthesis can be applied at much lower temperatures in shorter durations due to the high reactivity of plasma species [24–26]. More importantly, plasma can introduce abundant defects and porosity that favor electrochemical processes. Starting from $Ni(OH)_2$@glucose solid–liquid precursor, we are able to convert $Ni(OH)_2$ into porous Ni_2P and simultaneously decompose glucose into carbon that readily coats on the surface of the gradually formed Ni_2P particles using PH_3/He plasma to obtain Ni_2P@C core shell structures. Unlike conventional subsequent carbon coating strategy, our approach effectively prevents the Ni_2P from oxidation and thus maintains a high electric conductivity (Fig. S1 in the Electronic Supplementary Material (ESM)). More interestingly, the unique plasma process also produces phosphorus-rich nickel phosphides on the surface, which contribute significantly to the sodium storage capacity. Meanwhile, the confinement of monodispersive Ni_2P particles into carbon buffers the volumetric expansion of Ni_2P upon cycling. As a result, the phosphorus-rich Ni_2P@C electrodes deliver a high capacity of 693 mAh·g^{-1} after 50 cycles at 100 mA·g^{-1} along with outstanding stability (104 mAh·g^{-1} for at least 1,500 cycles at 2 A·g^{-1}).

2 Experimental section

2.1 Plasma synthesis of Ni_2P@C nanosheets

$Ni(OH)_2$ nanosheets were first synthesized by hydrothermally reacting 2 mmol $Ni(NO_3)_2·6H_2O$ with 4 mmol hexamethylenetetramine (HMT) at 100 °C for 10 h using a carbon paper as substrate. The as-obtained product was immersed into a glucose solution (80 mL, 0.1 mol·L^{-1}) for 3 h and then subjected to PH_3/He (1:9 in volumetric ratio, gas flow: 50 standard cubic centimeters per minute (sccm)) plasma treatment at 600 °C for 1 h with a plasma power of 200 W and a base pressure of 600 mTorr to get the Ni_2P@C nanosheets. For comparison, Ni_2P nanosheets without carbon coating shells were also synthesized by direct plasma conversion of $Ni(OH)_2$ precursor.

2.2 Characterizations

X-ray diffraction (XRD) patterns were recorded on a Bruker D8 Advance X-ray diffractometer using Cu Kα radiation. The morphology and structure were observed by scanning electron microscopy (SEM, FEI Nova Nano 630) and transmission electron microscopy (TEM, FEI Titan CM30). Raman spectra were collected using a Hariba LabRAM HR spectrometer. X-ray photoelectron spectroscopy (XPS) measurements were conducted using an Amicus ECSA 3400 XPS with Al Kα radiation.

2.3 Electrochemical measurements

The Ni_2P@C nanosheets on carbon paper were directly used as the working electrode and a sodium foil was used as the counter electrode. The loading of the Ni_2P@C electrode was about 2 mg·cm^{-2}. The two electrodes were placed face-to-face with a separator (Celgard 3501 microporous membrane) in between to assemble the CR2032-type coin cells. The electrolyte was 1 M $NaClO_4$ in a mixture of ethylene carbonate (EC)–dimethyl carbonate (DMC) with 1:1 weight ratio. The cell assembling was conducted in an argon-filled glove box with H_2O/O_2 concentration less than 1 ppm. The cyclic voltammetry (CV) measurements were performed on a Biologic VMP3 potentiostat within the voltage window of 0.01–3.0 V vs. Na/Na^+ at a scan rate of 0.1 mV·s^{-1}. The galvanostatic charge–discharge (GCD) tests were carried out on an Arbin BT-2043 battery testing system at different current densities under room temperature. Electrochemical impedance spectroscopy (EIS) was measured by applying a sine wave with an amplitude of 5 mV over the frequency from 100 kHz to 10 mHz at open-circuit voltage (OCV). The specific capacity was calculated based on the mass of the active material (Ni_2P@C).

3 Results and discussion

3.1 Structure and composition characteristics

The Ni_2P@C nanosheets were synthesized through a plasma conversion using our recently developed procedure [27]. Figure 1(a) illustrates the synthesis process of the Ni_2P@C nanosheets. $Ni(OH)_2$ nanosheets were first hydrothermally deposited onto a carbon paper substrate (see Experimental section for details) and then immersed into a glucose solution for 3 h, which allowed the glucose molecules to be adsorbed onto the surface of the nanosheets, forming $Ni(OH)_2$@glucose core shell structures. The resulting product was then subjected to PH_3/He plasma treatment. Upon this process, the inner core $Ni(OH)_2$ was converted to Ni_2P, whereas the outer shell glucose was simultaneously decomposed into carbon and uniformly coated on the surface of Ni_2P, eventually giving the porous Ni_2P@C core shell structures. For comparison, we also synthesized Ni_2P nanosheets by directly converting $Ni(OH)_2$ precursor using plasma. Figures 1(b) and 1(c) show the SEM images of the as-obtained Ni_2P, where well-defined nanosheets with smooth surface are interconnected to form a hierarchical network, well preserving the original morphology of the $Ni(OH)_2$ precursor (Fig. S2 in the ESM). The Ni_2P@C also exhibits a sheet-like morphology (Fig. 1(d)); however, the surface of these nanosheets is considerably rough, unlike the carbon shell formed by the routine process reported in literature [28]. A zoom-in SEM image reveals that there are in fact many tiny particles anchored on the surface (Fig. 1(e)), which we tentatively attributed to the phosphorus-rich nickel phosphide (NiP_x) nanoparticles and will be discussed later. Because of the change in crystal density during the phase conversion of $Ni(OH)_2$ to Ni_2P (from 4.1 to 7.44 g·cm^{-3}), porosity was introduced to the nanosheets, which has also been observed in

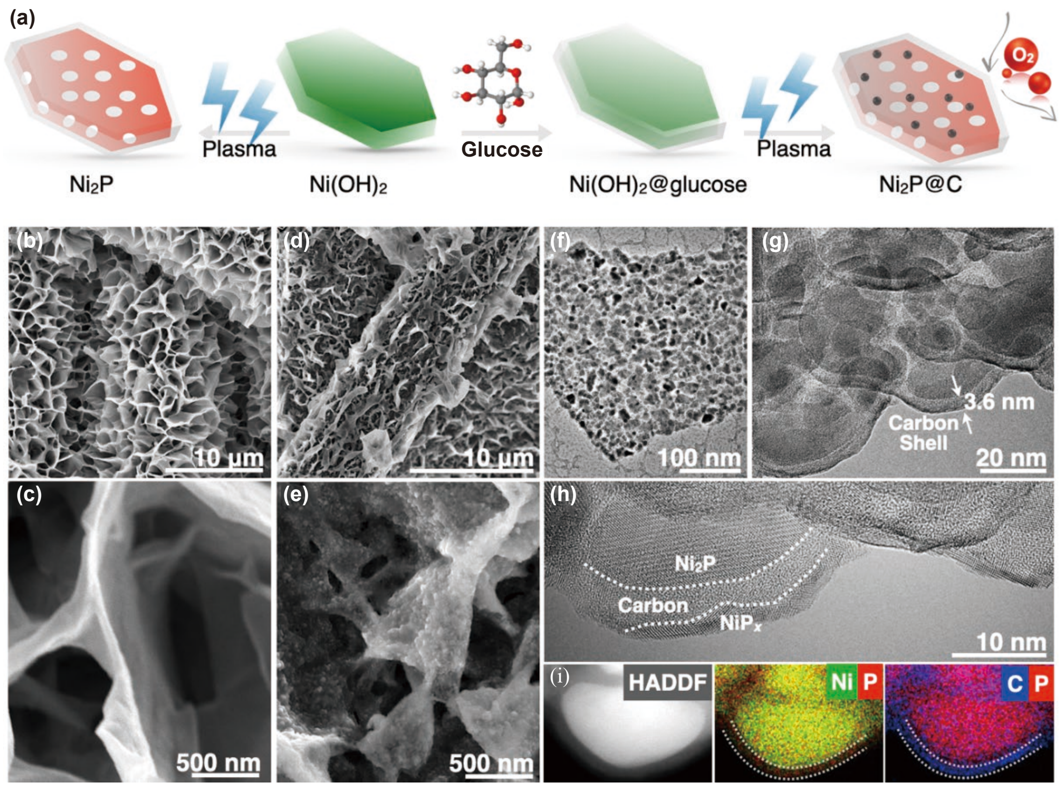

Figure 1 (a) Schematic illustration of the synthesis process of Ni_2P and Ni_2P@C nanosheets. (b) and (c) SEM images of Ni_2P nanosheets. ((d) and (e)) SEM, ((f) and (g)) TEM, (h) HRTEM images, and (i) elemental mapping images of Ni_2P@C nanosheets.

other metal hydroxide/phosphide systems [29, 30] and was confirmed by the TEM observations (Fig. 1(f)). A further magnified TEM image clearly suggests the core shell structure (Fig. 1(g)), where the carbon shell is light in contrast and the Ni_2P is dark in contrast. These Ni_2P nanoparticles are monodispersed and segregated from each other by the carbon shells. It is known that plasma is a partially ionized gas that contains electrons, ions, and other species (e.g., molecules, radicals, and photons). The mobility of electrons is much higher than that of other plasma species, and therefore the newly formed nanoparticles in the plasma are negatively charged. This prevents nanoparticles from agglomeration, which is a common problem facing those particles prepared by conventional thermal methods. The confinement of Ni_2P particles into flexible carbon can effectively increase the contact area and consequently alleviate the stress caused by Na^+ ion insertion. The thickness of the carbon shell is around 4 nm. Such a thin layer can buffer the volumetric change but without sacrificing the efficiency of Na^+ ion diffusion. Figure 1(h) shows the high-resolution TEM (HRTEM) image of the Ni_2P@C, where the interface between carbon and Ni_2P can be identified. Many nanoparticles on the carbon shell are also seen, which matches the SEM observation. The energy dispersive X-ray spectroscopy (EDS) elemental maps clearly reveal a phosphorus-rich layer on the surface (Fig. 1(i)), indicating the surface nanoparticles are phosphorus-rich nickel phosphides (NiP_x). This perhaps is not surprising given the plasma conversion is a progressive process from the surface to the inside [31]. The surface of the precursor would be attacked by high concentration of phosphine plasma ions and thus tends to form phosphorus-rich phases, whereas the inside forms metal-rich phases. Phosphorus-rich phases can deliver high sodium capacity [12] but are generally much more difficult to be synthesized by conventional reactions, as their formation requires high nucleation energy and harsh conditions (e.g., high temperature/pressure) [32], which, however, become much less an issue under the high-energy plasma ambient. It is worth mentioning that from the HRTEM of Ni_2P@C, we did not observe a surface metal phosphate layer that is commonly seen for Ni_2P and metal phosphides in general (Fig. S3 in the ESM). This result suggests that our unique simultaneous Ni_2P forming and carbon coating process can effectively protect the Ni_2P from oxidation, which is further confirmed by Raman results.

Even though the XRD patterns of Ni_2P@C and the Ni_2P control are almost identical (Fig. S4 in the ESM), their Raman spectra, however, are completely different from each other (Fig. 2(a)). It is well-known that metal phosphides are easily oxidized even upon air exposure and the surface phosphate layer is commonly observed for these materials as confirmed by our TEM results (Fig. S3 in the ESM) and literature [29, 33]. Therefore, the distinguished Raman spectra indicate their different oxidation behaviors. The Raman spectrum of Ni_2P@C shows typical Raman peaks of Ni_2P. The pristine Ni_2P also shows the characteristic A1' and E' peaks. However, a tiny shift is observed compared with the spectrum of Ni_2P@C, indicating the modified electronic properties after carbon coating. In addition, the Raman spectrum of pristine Ni_2P reveals several new peaks that might be associated with the nickel phosphates and oxides. These findings strongly confirm the excellent air stability of Ni_2P@C and the efficacy of our strategy of simultaneous carbon coating to prevent the oxidation of Ni_2P. The Raman spectrum of Ni_2P@C also shows two peaks at ~ 1,365 and ~ 1,582 cm^{-1} with significantly higher intensity as compared to those of pristine Ni_2P (with signal coming from the carbon paper substrate), corresponding to the disorder-induced phonon mode (D band) and graphite band (G band), respectively (Fig. 2(b)) [34]. This result confirms that glucose is decomposed into the carbon layer. The surface chemistry of Ni_2P@C was further investigated using XPS along with Ni_2P for comparison. The Ni 2p spectrum (Fig. 2(c)) of pristine Ni_2P shows two intense peaks at binding energies of 853.6 ($2p_{3/2}$) and 870.7 eV ($2p_{1/2}$), consistent with the reported values for nickel phosphides [35]. The peak located at 856.8 eV is attributed to the surface oxidized Ni phosphate/oxide layer [30]. In contrast, the intensity of the peaks observed for Ni_2P@C significantly reduces, which is due to the carbon coating

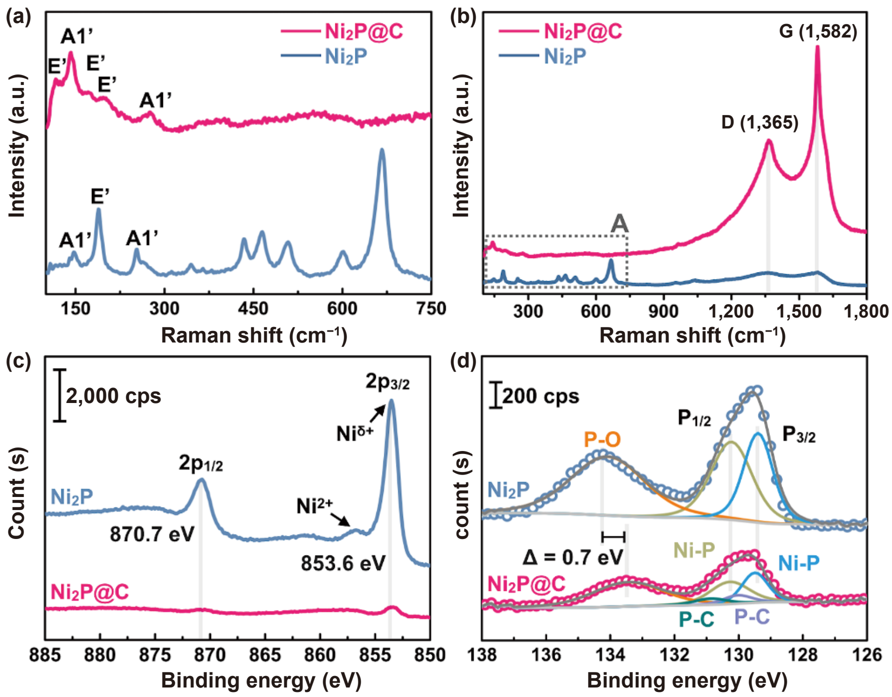

Figure 2 Structural characterization of Ni_2P and $Ni_2P@C$ nanosheets. (a) and (b) Raman spectra. (c) Ni 2p and (d) P 2p XPS spectra.

layer that attenuates the XPS signal collected from the inner Ni_2P. As for P 2p (Fig. 2(d)), the peak fitting analysis reveals two distinct P species in the pristine Ni_2P that can be identified as $P^{\delta-}$ in the form of phosphide ($2p_{3/2}$ and $2p_{1/2}$ peaks at 129.4 and 130.2 eV, respectively) and P^{5+} in the form of phosphate species (134.3 eV) [35]. The P 2p spectrum of $Ni_2P@C$ shows two doublets that can be assigned to Ni–P ($2p_{3/2}$ and $2p_{1/2}$ components at 129.5 and 130.3 eV) and P–C ($2p_{3/2}$ and $2p_{1/2}$ components at 130.0 and 130.9 eV) bonds, respectively [36]. The slight peak shift (0.1 eV) is likely caused by electronic interactions between the surface phosphorus and carbon. The peak at 133.6 eV might be associated with the oxidation of trace amount of the residual phosphorus on the surface of $Ni_2P@C$. Note that the Ni XPS signal of $Ni_2P@C$ is significantly reduced as compared to pristine Ni_2P; the P signal, however, is comparable, confirming a phosphorus-rich surface state. The quantification of the XPS results further indicates that the surface P:Ni ratio of $Ni_2P@C$ is 6.1:1. These results suggest the existence of phosphorus-rich nickel phosphides in $Ni_2P@C$ and explain the tiny nanoparticles observed in SEM and TEM. It is interesting to note that we did not observe phosphide-rich phases in pristine Ni_2P, which is further confirmed by the EDS analysis. The ratio of Ni:P in Ni_2P is 2.1:1, close to the stoichiometric ratio, whereas is 1.5:1 in $Ni_2P@C$ (Fig. S5 in the ESM). This might be due to the carbon layer with high surface area that adsorbs more PH_3 ions and thus promotes the formation of phosphide-rich phases in $Ni_2P@C$. These phosphorus-rich nickel phosphide (NiP_x) nanoparticles are expected to significantly boost the capacity of $Ni_2P@C$, especially compared to various structures of Ni_2P synthesized by conventional time-consuming routes such as vapor phase methods [35, 37], which are unlikely to produce NiP_x particles under similar conditions.

3.2 Electrochemical performance

We then investigated the Na^+ storage performance of $Ni_2P@C$ nanosheets by assembling them into CR2032-type coin cells with sodium foils as the reference and the counter electrodes (see details in Experimental section). Figure 3(a) compares the first two CV curves of $Ni_2P@C$ and Ni_2P nanosheets over the potential window of 0.01–3.0 V collected at 0.1 $mV \cdot s^{-1}$. In the first cathodic scan, two prominent peaks are observed at around 1.12 and 0.39 V for both electrodes, respectively. The former is related to the following conversion reaction.

$$Ni_2P + 3Na^+ + 3e^- \rightarrow Ni + Na_3P \quad (1)$$

But the latter is most likely associated with the formation of solid-electrolyte interface (SEI) film since it disappears in the subsequent cycle. As for the anodic scan, the peak at around 2.32 V corresponds to the desodiation process. Compared with Ni_2P, the redox peaks of $Ni_2P@C$ are more intense, which suggests that the $Ni_2P@C$ can store a larger amount of Na^+ ions. We further evaluated the cycling performance of the $Ni_2P@C$ and Ni_2P at a low current density of 100 $mA \cdot g^{-1}$. As shown in Fig. 4(b), the reversible capacity of $Ni_2P@C$ electrodes reaches 693 $mAh \cdot g^{-1}$ after 50 cycles, which is more than twice that of Ni_2P (269 $mAh \cdot g^{-1}$). It is noted that such high capacity exceeds the theoretical number of Ni_2P (542 $mAh \cdot g^{-1}$), which perhaps is not surprising given the phosphorus-rich nickel phosphide compounds (NiP_x) on the surface of $Ni_2P@C$ electrodes (for example, the theoretical capacity of NiP_3 is 1,587 $mAh \cdot g^{-1}$). Further, the plasma treatment is known to produce atomic-scale vacancies and nanoscale porosity in the samples due to the sputtering effect of the plasma ions [31]. These defects and nanovoids can facilitate insertion of more sodium ions and improve the sodiation capacity [38, 39]. In addition, the glucose-derived carbon could also contribute to the capacity. The initial Coulombic efficiency (CE) of $Ni_2P@C$ is 64%. The low CE could be attributed to the irreversible formation of SEI layer on the surface, especially for the high surface area carbon. In contrast, the first CE of Ni_2P is only 49%. The difference in CEs of the two electrodes upon the following cycles is shown in Fig. S6 in the ESM. The $Ni_2P@C$ possesses stable CEs of more than 99% after 12 cycles, whereas the CEs of Ni_2P are always lower, indicating the instable SEI layer. The rate performances of the two anodes were also examined by cycling the cells at an initial current density of 100 $mA \cdot g^{-1}$ with stepwise increase to high discharge/charge rates of 1,000 $mA \cdot g^{-1}$ (Fig. 3(c)). The $Ni_2P@C$ can deliver average capacities of 1,381, 722, 545, 365, 260, and 168 $mAh \cdot g^{-1}$ at 0.1, 0.2, 0.3, 0.5, 0.8, and 1.0 $A \cdot g^{-1}$, respectively. The Ni_2P also exhibits reasonable rate performance thanks to the nanosheet structure

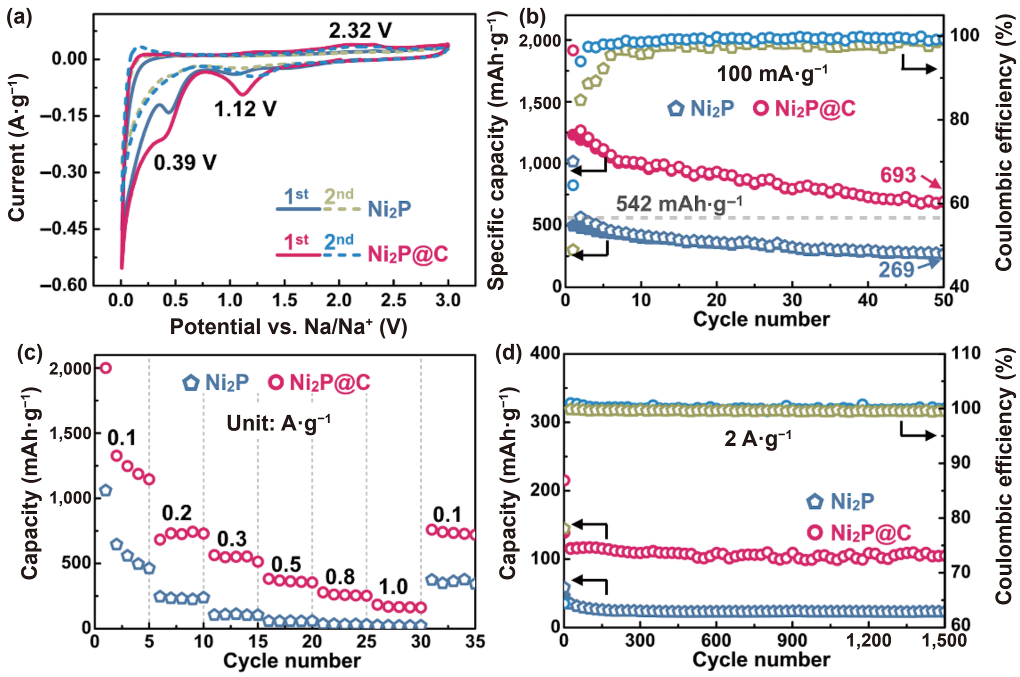

Figure 3 Comparison between the electrochemical Na^+ storage performance of Ni_2P and Ni_2P@C nanosheets. (a) CV curves of the first two cycles at a scan rate of 0.1 $mV·s^{-1}$. (b) Cycling performance at a current density of 100 $mA·g^{-1}$. (c) Rate performance at various current densities from 0.1 to 1.0 $A·g^{-1}$. (c) Long-term cycling performance at a current density of 2 $A·g^{-1}$.

that alleviates the large volumetric change upon cycling. The average capacities achieved on Ni_2P anodes at 0.1, 0.2, 0.3, 0.5, 0.8, and 1.0 $A·g^{-1}$ are 644, 234, 106, 57, 32, and 24 $mAh·g^{-1}$, respectively. These capacities compare favorably with other reported phosphides such as Cu_3P [21], however, are remarkably lower than those of Ni_2P@C (also see a comparison in Table S1 in the ESM). For example, the reversible capacity of the Ni_2P@C recovers to 736 $mAh·g^{-1}$ when the current density reduces to 100 $mA·g^{-1}$, almost twice as that of Ni_2P (361 $mAh·g^{-1}$). The superiority of the Ni_2P@C was further confirmed by the cycle performance at a high current density of 2 $A·g^{-1}$ (Fig. 3(d)). The capacity remains at ~ 104 $mAh·g^{-1}$ (corresponding to a capacity retention of 77%) even after 1,500 cycles, significantly higher than that of pristine Ni_2P (23 $mAh·g^{-1}$, corresponding to a capacity retention of 58%). These results strongly confirm the efficacy of our strategy of boosting the capacity and enhancing the stability by simultaneously converting $Ni(OH)_2$ into Ni_2P porous nanosheets and coating with carbon shells. As we discussed earlier, the electroactive Ni_2P nanoparticles are monodispersively confined within the carbon shells (Fig. 1(g)). Such unique structure not only effectively buffers the large volumetric change without significantly sacrificing the capacity upon cycling, but also creates interconnected conductive paths between individual Ni_2P particles that favor the fast electron transfer. This is also evidenced by the EIS measurements (Fig. S7 in the ESM). Both the Ni_2P@C and Ni_2P show a compressed semicircle within the high frequency range and a straight line inclined at approximately 45° within the low frequency range. The former is associated with the charge transfer resistance (R_{ct}) whereas the latter is considered as Warburg impedance [31]. The much smaller radius of the semicircle of Ni_2P@C indicates a much lower charge transfer resistance, suggesting enhanced electrode kinetics [32, 33]. As mentioned above, the carbon shell can protect the Ni_2P from oxidation, enhance the conductivity of Ni_2P, and prevent the aggregation of nanoparticles.

We then conducted electrochemical kinetics analysis to further examine the superior performance of Ni_2P@C electrodes. The charge storage in electrode materials can be generally categorized into two types: the faradaic contribution from redox reaction and the non-Faradaic contribution from double-layer capacitance [40]. The faradaic contribution includes two components: the diffusion-controlled Na^+ ion insertion into the bulk of materials (traditional batteries), and the redox pseudocapacitive process that takes place at or near the surface of the active materials. These effects then can be characterized by analyzing the CV data at various sweep rates according to [41]

$$i = av^b \tag{2}$$

where the current i obeys a power law relationship with the sweep rate v and a is a constant. The b value can be determined from the slope of the plot of log i vs. log v and therefore serves as an indicator of the charge storage type. The current is diffusion-controlled if $b = 0.5$, whereas it is capacitive responsed if $b = 1$. We then collected the CV data (after the 1st cycle) of the Ni_2P@C (Fig. 4(a)) and Ni_2P (Fig. S8 in the ESM) electrodes at different scan rates. Both materials show a pair of redox peaks, and the cathodic and anodic peaks merely shift even at high scan rates, especially for the Ni_2P@C nanosheets, which is one of the typical pseudocapacitive behaviors [42]. The b values were then determined using the CV data. As shown in Fig. 4(b), the b values for both materials are within 0.5–0.8, which implies that the current response arises from both capacitive reaction and diffusion-controlled Na^+ ion insertion. The b values of Ni_2P@C approach 0.8 in the whole voltage window, indicating the charge storage in Ni_2P@C is mostly dominated by the capacitive behavior. Noticeably, the b values (approaching 0.5) of Ni_2P are always lower than those of Ni_2P@C, reflecting a rate-limited Na^+ insertion process. To further distinguish quantitatively the capacitive contribution to the current response, we then expressed the current (i) at a fixed potential (V) as being the combination of capacitive effects (k_1v) and diffusion-controlled insertion processes ($k_2v^{1/2}$) according to [43]

$$i(V) = k_1v + k_2v^{1/2} \tag{3}$$

For analytical purposes, the above equation can be rearranged to

$$i(V)/v^{1/2} = k_1v^{1/2} + k_2 \tag{4}$$

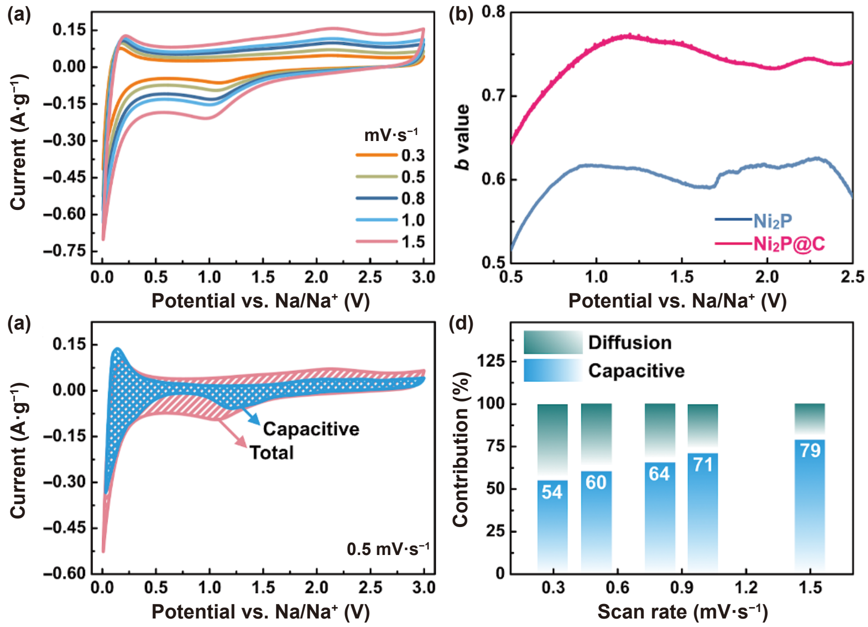

Figure 4 Reaction kinetics and quantitative analysis of the Na^+ storage mechanism on Ni_2P@C nanosheets. (a) CV curves after the 1st cycle recorded at various scan rates from 0.3 to 1.5 $mV \cdot s^{-1}$. (b) *b* values at different potentials. (c) Diffusion-controlled and capacitive contributions to the charge storage at 0.5 $mV \cdot s^{-1}$. (d) Normalized contribution ratio of the diffusion-controlled and capacitive capacities at different scan rates.

The parameters k_1 and k_2 can then be easily determined by plotting $i(V)/v^{1/2}$ against $v^{1/2}$, which allow to quantify the fraction of each contribution to the current. Figure 4(c) shows the capacitive current response (indicated as blue shaded area) in contrast to the total current (red shaded area) of Ni_2P@C electrodes obtained at 0.5 $mV \cdot s^{-1}$. The capacitive response is clearly the major contribution (60%) to the total current of Ni_2P@C, especially around the peak regions. Likewise, the fraction of the current due to each of these contributions (e.g. capacitive and diffusion-controlled) at various scan rates can be also quantified and is summarized in Fig. 4(d). The result shows that for Ni_2P@C, the capacitive contribution gradually increases with the increasing scan rate (from 54% at 0.3 $mV \cdot s^{-1}$ to 79% at 1.5 $mV \cdot s^{-1}$). On the contrary, the capacitive contribution in Ni_2P is much lower. For example, merely 37% of current response (at 0.5 $mV \cdot s^{-1}$) of pristine Ni_2P is controlled by the capacitive behavior (Fig. S9 in the ESM). This result confirms that the carbon shell is critical for the capacitive behavior observed for Ni_2P@C. The investigations mentioned above yield a whole picture of Ni_2P@C as an anode material for sodium ion batteries. The existence of surface phosphorus-rich NiP_x gives a high Na^+ storage capacity, whereas the *in situ* formed carbon shell effectively prevents the Ni_2P nanoparticles from oxidation. These factors together result in a much higher capacity of the Ni_2P@C as compared with other reported Ni_2P electrodes. In addition, the carbon shell also improves the intrinsic conductivity as well as relieves the volumetric variation, thus leading to good stability.

4 Conclusions

In conclusion, we developed a plasma method to synthesize porous Ni_2P@C core shell nanosheets for high performance sodium ion battery anode materials. Starting from $Ni(OH)_2$@glucose precursor, we were able to convert $Ni(OH)_2$ into porous Ni_2P nanosheets and simultaneously coat them with carbon shell using PH_3/He plasma. Unlike traditional subsequent carbon coating strategy, our approach could effectively prevent the phosphide materials from oxidation and thus maintain a high electric conductivity of Ni_2P. The confinement of monodispersive Ni_2P nanoparticles into carbon alleviates the volumetric expansion of Ni_2P without deforming the carbon shell or disrupting the SEI on the surface. Furthermore, the unique plasma treatment also produces phosphorus-rich nickel phosphides on the surface of Ni_2P@C, and nanoscale porosity and atomic-scale vacancies that are unlikely achieved by other conventional methods. In this way, a high capacity of 693 $mAh \cdot g^{-1}$ after 50 cycles at a current density of 100 $mA \cdot g^{-1}$ is achieved. Meanwhile, 104 $mAh \cdot g^{-1}$ (77% capacity retention) can be retained for at least 1,500 cycles at a high rate of 2 $A \cdot g^{-1}$, which is rarely achieved among many other phosphide electrodes. Our work not only presents a plasma route to the metal phosphide/carbon core shell nanostructures, but also provides a general strategy of constructing high performance anodes for conversion type electrode materials that have high capacity but commonly suffer from poor stability because of the large volumetric changes upon cycling.

Acknowledgments

This work was supported by the National Natural Science Foundation of China (Nos. 21805136 and 22001081), the Startup Foundation for Introducing Talent of NUIST (Nos. 1521622101002 and 1521622101003), and the open research fund of State Key Laboratory of Organic Electronics and Information Displays.

Electronic Supplementary Material: Supplementary material (aditional characterizations on structures and electrochemical performances of the materials) is available in the online version of this article at https://doi.org/10.1007/s12274-021-3738-8.

References

[1] Lu, L. G.; Han, X. B.; Li, J. Q.; Hua, J. F.; Ouyang, M. G. A review on the key issues for lithium-ion battery management in electric vehicles. *J. Power Sources* **2013**, *226*, 272–288.

[2] Etacheri, V.; Marom, R.; Elazari, R.; Salitra, G.; Aurbach, D. Challenges in the development of advanced Li-ion batteries: A review. *Energy Environ. Sci.* **2011**, *4*, 3243–3262.

[3] Dunn, B.; Kamath, H.; Tarascon, J. M. Electrical energy storage for the grid: A battery of choices. *Science* **2011**, *334*, 928–935.

[4] Chen, K. F.; Yin, S.; Xue, D. F. Active La-Nb-O compounds for fast lithium-ion energy storage. *Tungsten* **2019**, *1*, 287–296.

[5] Liu, X. Q.; Li, L. P.; Li, G. S. Partial surface phase transformation of Li_3VO_4 that enables superior rate performance and fast lithium-ion storage. *Tungsten* **2019**, *1*, 276–286.
[6] Slater, M. D.; Kim, D.; Lee, E.; Johnson, C. S. Sodium-ion batteries. *Adv. Funct. Mater.* **2013**, *23*, 947–958.
[7] Yabuuchi, N.; Kubota, K.; Dahbi, M.; Komaba, S. Research development on sodium-ion batteries. *Chem. Rev.* **2014**, *114*, 11636–11682.
[8] Su, X.; Wu, Q. L.; Li, J. C.; Xiao, X. C.; Lott, A.; Lu, W. Q.; Sheldon, B. W.; Wu, J. Silicon-based nanomaterials for lithium-ion batteries: A review. *Adv. Energy Mater.* **2014**, *4*, 1300882.
[9] Kim, S. W.; Seo, D. H.; Ma, X. H.; Ceder, G.; Kang, K. Electrode materials for rechargeable sodium-ion batteries: Potential alternatives to current lithium-ion batteries. *Adv. Energy Mater.* **2012**, *2*, 710–721.
[10] Yang, F. H.; Gao, H.; Chen, J.; Guo, Z. P. Phosphorus-based materials as the anode for sodium-ion batteries. *Small Methods* **2017**, *1*, 1700216.
[11] Song, J. X.; Yu, Z. X.; Gordin, M. L.; Hu, S.; Yi, R.; Tang, D. H.; Walter, T.; Regula, M.; Choi, D.; Li, X. L. et al. Chemically bonded phosphorus/graphene hybrid as a high performance anode for sodium-ion batteries. *Nano Lett.* **2014**, *14*, 6329–6335.
[12] Sun, M.; Liu, H. J.; Qu, J. H.; Li, J. H. Earth-rich transition metal phosphide for energy conversion and storage. *Adv. Energy Mater.* **2016**, *6*, 1600087.
[13] Kim, Y.; Ha, K. H.; Oh, S. M.; Lee, K. T. High-capacity anode materials for sodium-ion batteries. *Chem. Eur. J.* **2014**, *20*, 11980–11992.
[14] Liang, H. F.; Xia, C.; Jiang, Q.; Gandi, A. N.; Schwingenschlögl, U.; Alshareef, H. N. Low temperature synthesis of ternary metal phosphides using plasma for asymmetric supercapacitors. *Nano Energy* **2017**, *35*, 331–340.
[15] Zhou, K.; Zhou, W. J.; Yang, L. J.; Lu, J.; Cheng, S.; Mai, W.; Tang, Z. H.; Li, L. G.; Chen, S. W. Ultrahigh-performance pseudocapacitor electrodes based on transition metal phosphide nanosheets array via phosphorization: A general and effective approach. *Adv. Funct. Mater.* **2015**, *25*, 7530–7538.
[16] Feng, Y. Y.; Zhang, H. J.; Mu, Y. P.; Li, W. X.; Sun, J. L.; Wu, K.; Wang, Y. Monodisperse sandwich-like coupled quasi-graphene sheets encapsulating Ni_2P nanoparticles for enhanced lithium-ion batteries. *Chem. Eur. J.* **2015**, *21*, 9229–9235.
[17] Bai, Y. J.; Zhang, H. J.; Fang, L.; Liu, L.; Qiu, H. J.; Wang, Y. Novel peapod array of Ni_2P@ graphitized carbon fiber composites growing on Ti substrate: A superior material for Li-ion batteries and the hydrogen evolution reaction. *J. Mater. Chem. A* **2015**, *3*, 5434–5441.
[18] Lu, Y.; Tu, J. P.; Xiong, Q. Q.; Qiao, Y. Q.; Zhang, J.; Gu, C. D.; Wang, X. L.; Mao, S. X. Carbon-decorated single-crystalline Ni_2P nanotubes derived from Ni nanowire templates: A high-performance material for Li-ion batteries. *Chem. Eur. J.* **2012**, *18*, 6031–6038.
[19] Lu, Y.; Wang, X. L.; Mai, Y. J.; Xiang, J. Y.; Zhang, H.; Li, L.; Gu, C. D.; Tu, J. P.; Mao, S. X. Ni_2P/graphene sheets as anode materials with enhanced electrochemical properties versus lithium. *J. Phys. Chem. C* **2012**, *116*, 22217–22225.
[20] Bai, Y. J.; Zhang, H. J.; Li, X.; Liu, L.; Xu, H. T.; Qiu, H. J.; Wang, Y. Novel peapod-like Ni_2P nanoparticles with improved electrochemical properties for hydrogen evolution and lithium storage. *Nanoscale* **2015**, *7*, 1446–1453.
[21] Xia, Q. B.; Li, W. J.; Miao, Z. C.; Chou, S. L.; Liu, H. K. Phosphorus and phosphide nanomaterials for sodium-ion batteries. *Nano Res.* **2017**, *10*, 4055–4081.
[22] Fan, M. P.; Chen, Y.; Xie, Y. H.; Yang, T. Z.; Shen, X. W.; Xu, N.; Yu, H. Y.; Yan, C. L. Half-cell and full-cell applications of highly stable and binder-free sodium ion batteries based on Cu_3P nanowire anodes. *Adv. Funct. Mater.* **2016**, *26*, 5019–5027.
[23] Wang, X. J.; Chen, K.; Wang, G.; Liu, X. J.; Wang, H. Rational design of three-dimensional graphene encapsulated with hollow FeP@carbon nanocomposite as outstanding anode material for lithium ion and sodium ion batteries. *ACS Nano* **2017**, *11*, 11602–11616.
[24] Li, Q.; Li, X. R.; Gu, J. W.; Li, Y. L.; Tian, Z. Q.; Pang, H. Porous rod-like Ni_2P/Ni assemblies for enhanced urea electrooxidation. *Nano Res.* **2021**, *14*, 1405–1412.
[25] Zhou, H. J.; Zheng, M. B.; Pang, H. Synthesis of hollow amorphous cobalt phosphide-cobalt oxide composite with interconnected pores for oxygen evolution reaction. *Chem. Eng. J.* **2021**, *416*, 127884.
[26] Zhang, G. X.; Li, Y. L.; Xiao, X.; Shan, Y.; Bai, Y.; Xue, H. -G.; Pang, H.; Tian, Z. Q.; Xu, Q. *In situ* anchoring polymetallic phosphide nanoparticles within porous prussian blue analogue nanocages for boosting oxygen evolution catalysis. *Nano Lett.* **2021**, *21*, 3016–3025.
[27] Liang, H. F.; Alshareef, H. N. A plasma-assisted route to the rapid preparation of transition-metal phosphides for energy conversion and storage. *Small Methods* **2017**, *1*, 1700111.
[28] Xia, C.; Zhang, F.; Liang, H. F.; Alshareef, H. N. Layered SnS sodium ion battery anodes synthesized near room temperature. *Nano Res.* **2017**, *10*, 4368–4377.
[29] Liang, H. F.; Gandi, A. N.; Anjum, D. H.; Wang, X. B.; Schwingenschlögl, U.; Alshareef, H. N. Plasma-assisted synthesis of NiCoP for efficient overall water splitting. *Nano Lett.* **2016**, *16*, 7718–7725.
[30] Liang, H. F.; Gandi, A. N.; Xia, C.; Hedhili, M. N.; Anjum, D. H.; Schwingenschlögl, U.; Alshareef, H. N. Amorphous NiFe-OH/NiFeP electrocatalyst fabricated at low temperature for water oxidation applications. *ACS Energy Lett.* **2017**, *2*, 1035–1042.
[31] Zhang, Y. Q.; Rawat, R. S.; Fan, H. J. Plasma for rapid conversion reactions and surface modification of electrode materials. *Small Methods* **2017**, *1*, 1700164.
[32] Carenco, S.; Portehault, D.; Boissiè, C.; Mézailles, N.; Sanchez, C. Nanoscaled metal borides and phosphides: Recent developments and perspectives. *Chem. Rev.* **2013**, *113*, 7981–8065.
[33] You, B.; Jiang, N.; Sheng, M. L.; Bhushan, M. W.; Sun, Y. J. Hierarchically porous urchin-like Ni_2P superstructures supported on nickel foam as efficient bifunctional electrocatalysts for overall water splitting. *ACS Catal.* **2016**, *6*, 714–721.
[34] Matthews, M. J.; Pimenta, M. A.; Dresselhaus, G.; Dresselhaus, M. S.; Endo, M. Origin of dispersive effects of the Raman *D* band in carbon materials. *Phys. Rev. B* **1999**, *59*, R6585–R6588.
[35] Panneerselvam, A.; Malik, M. A.; Afzaal, M.; O'Brien, P.; Helliwell, M. The chemical vapor deposition of nickel phosphide or selenide thin films from a single precursor. *J. Am. Chem. Soc.* **2008**, *130*, 2420–2421.
[36] Singh, K. P.; Bae, E. J.; Yu, J. -S. Fe–P: A new class of electroactive catalyst for oxygen reduction reaction. *J. Am. Chem. Soc.* **2015**, *137*, 3165–3168.
[37] Motojima, S.; Haguri, K.; Takahashi, Y.; Sugiyama, K. Chemical vapor deposition of nickel phosphide Ni_2P. *J. Less-Common Met.* **1979**, *64*, 101–106.
[38] Xu, J. T.; Wang, M.; Wickramaratne, N. P.; Jaroniec, M.; Dou, S. X.; Dai, L. M. High-performance sodium ion batteries based on a 3D anode from nitrogen-doped graphene foams. *Adv. Mater.* **2015**, *27*, 2042–2048.
[39] Xu, D. F.; Chen, C. J.; Xie, J.; Zhang, B.; Miao, L.; Cai, J.; Huang, Y. H.; Zhang, L. N. A Hierarchical N/S-codoped carbon anode fabricated facilely from cellulose/polyaniline microspheres for high-performance sodium-ion batteries. *Adv. Energy Mater.* **2016**, *6*, 1501929.
[40] Brezesinski, T.; Wang, J.; Tolbert, S. H.; Dunn, B. Ordered mesoporous α-MoO_3 with iso-oriented nanocrystalline walls for thin-film pseudocapacitors. *Nat. Mater.* **2010**, *9*, 146–151.
[41] Lindström, H.; Södergren, S.; Solbrand, A.; Rensmo, H.; Hjelm, J.; Hagfeldt, A.; Lindquist, S. -E. Li^+ ion insertion in TiO_2 (anatase). 2. Voltammetry on nanoporous films. *J. Phys. Chem. B* **1997**, *101*, 7717–7722.
[42] Dong, Y. F.; Wang, B. L.; Zhao, K. N.; Yu, Y. H.; Wang, X. D.; Mai, L. Q.; Jin, S. Air-stable porous Fe_2N encapsulated in carbon microboxes with high volumetric lithium storage capacity and a long cycle life. *Nano Lett.* **2017**, *17*, 5740–5746.
[43] Liu, T. C.; Pell, W. G.; Conway, B. E.; Roberson, S. L. Behavior of molybdenum nitrides as materials for electrochemical capacitors: Comparison with ruthenium oxide. *J. Electrochem. Soc.* **1998**, *145*, 1882–1888.